

ARTICLE

Open Access

# Biostable wireless sensor-integrated bioresorbable stent for real-time monitoring of vascular pressure and fractional flow reserve

Jinliang Wei<sup>1,2</sup>, Arunkumar Shanmugasundaram<sup>1,2</sup>, Nomin-Erdene Oyunbaatar<sup>1,2</sup>, Lei Wang<sup>1,2</sup> and Dong-Weon Lee<sup>1,2,3</sup>✉

## Abstract

Stent implantation is widely used to treat coronary artery disease, yet in-stent restenosis (ISR) remains a major clinical challenge. Fractional flow reserve (FFR) is the gold-standard index for evaluating restenosis severity, but current techniques are invasive and unsuitable for continuous monitoring. Here, we present a bioresorbable smart stent platform that enables real-time intravascular pressure sensing and continuous FFR monitoring. The system integrates a MEMS-based LC pressure sensor, fabricated from SU-8 and gold, onto a hybrid 3D-printed vascular stent composed of polycaprolactone (PCL) and polylactic acid (PLA). Structural refinements and an optimized fabrication process enable long-term sensor reliability, minimize signal drift, and maintain stable resonance frequency. Across 100 fabricated devices, the pressure sensors show a resonance frequency of  $82.2 \pm 1.7$  MHz and a sensitivity of  $37.48 \pm 2.13$  kHz/mmHg. In vitro closed-loop fluidic tests using a vascular phantom confirmed the stable, wireless operation of the device and its ability to accurately assess hemodynamic parameters. The dual-sensor configuration enables simultaneous upstream and downstream pressure measurements, yielding FFR values that closely match those from a commercial system ( $R^2 = 0.97$ ) under varying stenosis severities. The proposed smart stent offers a promising pathway toward long-term, non-invasive vascular monitoring and early detection of ISR.

Cardiovascular disease (CVD) is the leading cause of death worldwide, responsible for ~31% of all fatalities<sup>1–4</sup>. One of the main causes of CVD is atherosclerosis, where fibro-fatty plaques form within arterial walls and can lead to heart attack or stroke<sup>5–8</sup>. Stent implantation via percutaneous coronary intervention is widely used to reopen occluded vessels<sup>9,10</sup>. Over the years, stent technology has progressed from bare-metal to drug-eluting and bioresorbable designs<sup>11–17</sup>. Bioresorbable materials offer unique advantages over permanent metallic or polymeric stents because they gradually degrade after the vessel has healed, eliminating long-term foreign-body retention and

reducing the risk of late thrombosis and chronic inflammation<sup>18–20</sup>. Their transient presence also avoids secondary retrieval procedures and restores natural vascular compliance once the stent is resorbed, making them an attractive platform for next-generation vascular implants. Despite these advances, in-stent restenosis (ISR) remains a major complication<sup>21–25</sup>. Current ISR monitoring relies on angiography, intravascular ultrasound, optical coherence tomography, and fractional flow reserve (FFR), all of which require catheter-based vascular access. These methods are hospital-based interventions, costly, intermittent, and expose patients to contrast agents and radiation<sup>26–29</sup>. Consequently, a continuous, minimally invasive approach for real-time assessment of ISR and hemodynamics is highly desirable to enable timely intervention and improve patient comfort.

To address this need, implantable “smart stents” have been investigated for intravascular pressure and flow

Correspondence: Dong-Weon Lee ([mems@jnu.ac.kr](mailto:mems@jnu.ac.kr))

<sup>1</sup>MEMS and Nanotechnology Laboratory, School of Mechanical Engineering, Chonnam National University, Gwangju, Republic of Korea

<sup>2</sup>Advanced Medical Device Research Center for Cardiovascular Disease, Chonnam National University, Gwangju, Republic of Korea

Full list of author information is available at the end of the article

© The Author(s) 2026



**Open Access** This article is licensed under a Creative Commons Attribution-NonCommercial-NoDerivatives 4.0 International License, which permits any non-commercial use, sharing, distribution and reproduction in any medium or format, as long as you give appropriate credit to the original author(s) and the source, provide a link to the Creative Commons licence, and indicate if you modified the licensed material. You do not have permission under this licence to share adapted material derived from this article or parts of it. The images or other third party material in this article are included in the article's Creative Commons licence, unless indicated otherwise in a credit line to the material. If material is not included in the article's Creative Commons licence and your intended use is not permitted by statutory regulation or exceeds the permitted use, you will need to obtain permission directly from the copyright holder. To view a copy of this licence, visit <http://creativecommons.org/licenses/by-nc-nd/4.0/>.

monitoring<sup>30–33</sup>. However, most designs do not measure FFR, one of the most clinically validated metrics for assessing restenosis severity<sup>34–39</sup>. FFR is defined as the ratio of distal to proximal pressure across a stenosis under hyperemic conditions<sup>40–45</sup>. The inability of current smart stents to measure FFR arises from two main limitations. First, most stents integrate only a single pressure sensor, which cannot provide simultaneous proximal and distal measurements. Second, sensor stability is often compromised: accurate FFR requires highly reliable sensors with low noise, minimal drift, and consistent baseline resonance frequencies. Even small mismatches between two sensors can produce erroneous FFR values and false diagnoses<sup>46–50</sup>.

A primary cause of such drift in baseline is arising from the inconsistency in resonance frequency of the pressure sensors. The integrated pressure sensors typically employ a diaphragm–coil structure fabricated using photolithographic techniques and sealed through thermal bonding. During bonding, elevated temperatures and pressure differentials between the internal cavity and the external environment can induce deformation in both the diaphragm and coil structures. These deformations alter the inductance and capacitance of the LC circuit, resulting in unpredictable shifts in baseline resonance frequency. Even when multiple sensors are fabricated under identical process conditions, variations in deformation across devices often lead to noticeable differences in resonance frequencies and high tolerance values. Such variation in resonance frequency complicates direct comparison of sensor outputs and prevents accurate pressure differential calculation for FFR. Therefore, optimizing the sensor fabrication process to minimize mechanical deformation and ensure baseline frequency stability is critical for enabling accurate and reliable hemodynamic sensing and FFR monitoring in smart stent applications.

Herein, we propose a wireless pressure sensor-integrated hybrid bioresorbable vascular stent (BVS) for highly reliable and continuous FFR monitoring. The hybrid BVS, composed of polycaprolactone (PCL) and polylactic acid (PLA), was fabricated using a 3D printing technology. The wireless pressure sensor was fabricated through a modified photolithography process, with several design strategies implemented to mitigate structural deformation and enhance signal stability. The fabricated sensor exhibited an initial resonance frequency of  $82.2 \pm 1.7$  MHz and a sensitivity of  $37.48 \pm 2.13$  kHz/mmHg, as determined from the signal responses of 100 sensors. To evaluate its practical utility, the smart stent was implanted into a vascular phantom. The proposed smart stent demonstrated reliable detection of hemodynamic changes under control in vitro vascular phantom conditions. Specifically, the system was able to detect varying degrees of induced in-stent restenosis,

including 25%, 50%, and 75% luminal narrowing, through corresponding changes in pressure and FFR values. The FFR measurements obtained from the proposed smart stent closely matched those recorded by a commercial FFR system, validating its accuracy, stability, and clinical utility for continuous real-time hemodynamic monitoring.

## Results and discussion

The proposed smart stent integrates a 3D-printed bioresorbable hybrid polymer stent with wireless LC pressure sensors for continuous intravascular pressure monitoring and real-time FFR evaluation. Two sensors are strategically positioned at the proximal (Pa) and distal (Pd) ends of the stent to capture upstream and downstream pressures across the stenotic region (Fig. 1a). This dual-sensor configuration is critical for FFR calculation, which relies on the ratio of distal to proximal pressures under hyperemic conditions. Each wireless sensor, fabricated using MEMS technology, consists of an inductor coil and a fixed capacitor plate, coupled with a diaphragm incorporating a deformable capacitor plate and a sealed air cavity to transduce pressure into measurable frequency shifts (Fig. 1b). The principle of operation is based on the LC resonance mechanism, wherein variations in diaphragm deflection alter the capacitance of the circuit, thereby modulating the resonance frequency of the coil. These frequency changes are wirelessly transmitted to an external reader, enabling continuous and real-time monitoring without the need for tethered connections or invasive catheterization.

To ensure long-term stability, sensing reliability and stable resonance frequency shifts several structural refinements were incorporated into the sensor design. The top capacitor plate was deliberately enlarged beyond the diaphragm cavity, serving both as an electrical element and as a mechanical support bridge.

This structural modification suppresses thermally induced deformation of the SU-8 layer during bonding, a known challenge in conventional MEMS-based pressure sensors. Additionally, an open window was introduced into the press block to prevent localized compression of the coil during bonding, thereby maintaining the resonance characteristics of the LC circuit. An air-elimination channel was also integrated into the diaphragm to equilibrate pressure between the internal cavity and the external environment during bonding. This feature allows trapped air to escape, preventing undesirable deflection and improving device-to-device reproducibility.

The hybrid BVS was fabricated from PCL and PLA using high-resolution 3D printing, offering a balance of radial strength, flexibility, and controlled degradation. As shown in Fig. 1c, the BVS was initially crimped, after which the pressure sensors were attached via a mechanical coupling structure. To maintain flexibility and conformal

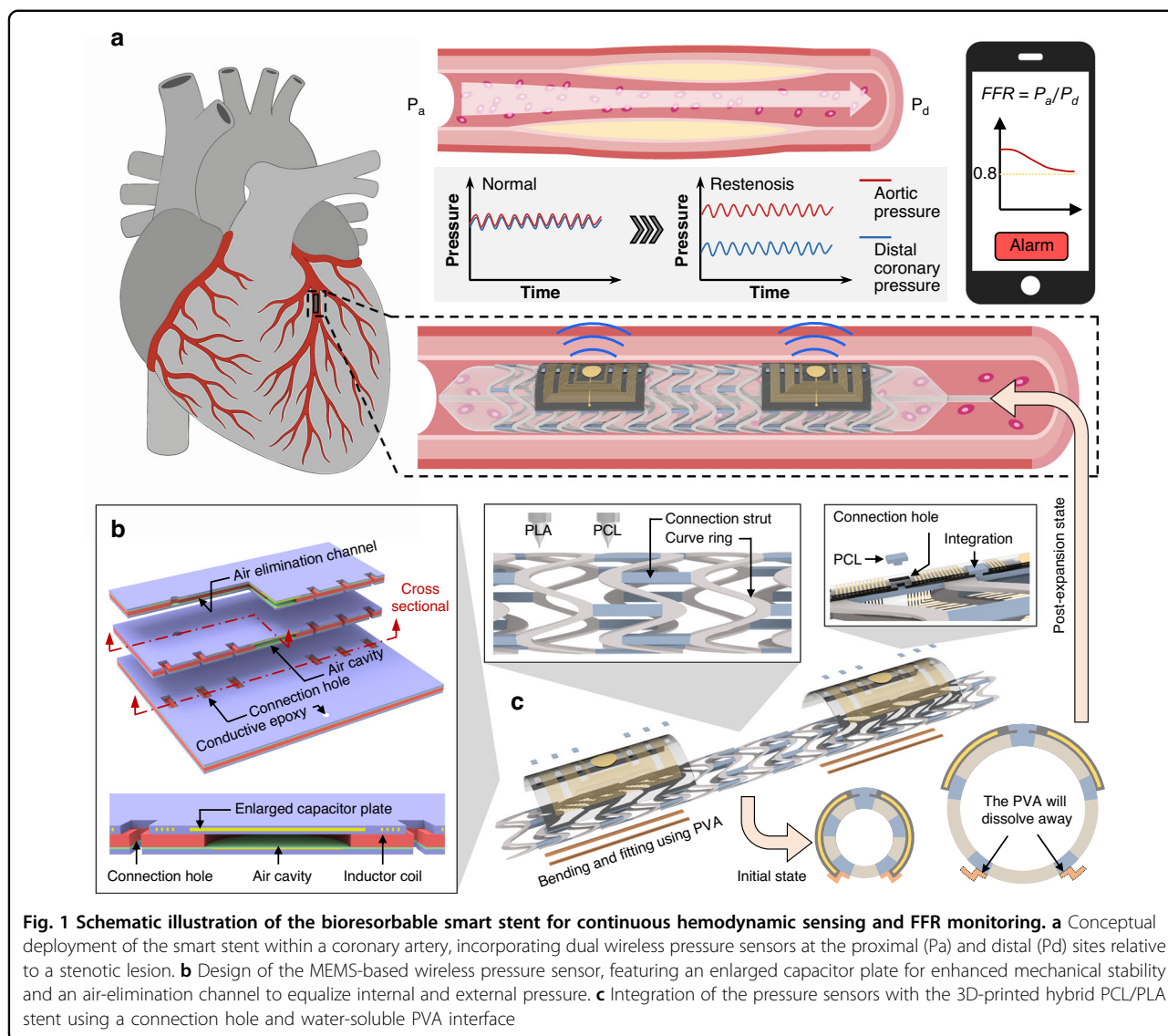


**Fig. 1 Schematic illustration of the bioresorbable smart stent for continuous hemodynamic sensing and FFR monitoring.** **a** Conceptual deployment of the smart stent within a coronary artery, incorporating dual wireless pressure sensors at the proximal ( $P_a$ ) and distal ( $P_d$ ) sites relative to a stenotic lesion. **b** Design of the MEMS-based wireless pressure sensor, featuring an enlarged capacitor plate for enhanced mechanical stability and an air-elimination channel to equalize internal and external pressure. **c** Integration of the pressure sensors with the 3D-printed hybrid PCL/PLA stent using a connection hole and water-soluble PVA interface

attachment, a thin biocompatible, water-soluble PVA layer was applied. This sacrificial PVA interface ensures stable fixation during deployment while dissolving post-implantation to restore natural vascular conformity. Additional thermal and mechanical analyses confirming that the PCL bonding temperature does not induce softening, deformation, or strength loss in PLA are provided in the Supporting Information (Fig. S1). The assembled smart stent was mounted on a balloon catheter and deployed into a vascular phantom model to validate its catheter compatibility and mechanical integrity under physiological conditions. By enabling implantable, wireless, and continuous hemodynamic monitoring, the proposed smart stent provides accurate FFR assessment in real time, representing a substantial improvement over current catheter-based methods, which are intermittent, costly, and invasive. The hybrid stent consists of materials with

different degradation behaviors that define its functional lifetime. The PCL/PLA stent undergoes hydrolytic resorption under physiological conditions, with PLA degrading over several months and PCL over a longer period, allowing the stent to gradually disappear after vascular healing and minimizing long-term foreign-body presence. In contrast, the SU-8 encapsulation layer and Au electrode are biostable and remain chemically intact during the monitoring period, as SU-8 resists hydrolysis and gold is corrosion-stable in physiological environments. Because the sensing module remains intact while the stent resorbs, the wireless sensor can be safely retrieved via standard percutaneous catheter techniques once vessel patency is restored. Beyond its immediate utility for in-stent restenosis surveillance, this platform offers a transformative pathway toward next-generation bioresorbable cardiovascular implants with integrated diagnostic capabilities.

In the initial fabrication of SU-8-based wireless pressure sensors without optimization, pronounced structural deformation was observed in both the coil and diaphragm capacitor plates (Fig. 2a). During thermal bonding at 150 °C, the SU-8 polymer softened and could not withstand the applied compressive forces, leading to approximately 10 µm inward collapse of the coil capacitor plate. At the same time, the diaphragm capacitor plate experienced approximately 6 µm inward deflection due to the pressure imbalance between the sealed internal cavity and the external environment during the cooling phase (Fig. S2). These deformations significantly affected the baseline resonance frequency of the LC circuit, introducing unpredictable drift and compromising both sensing accuracy and long-term stability. Importantly, even when multiple sensors were fabricated within the same batch, device-to-device variations remained high, primarily due to inconsistent deformation patterns (Fig. S3). Such instability is particularly problematic in dual-sensor FFR monitoring, where even small baseline mismatches between proximal and distal sensors can generate misleading diagnostic outcomes.

To overcome these challenges, three structural optimization strategies were systematically introduced. First, a laser-cut open window above the capacitor plate reduced the direct mechanical load during bonding, thereby mitigating compressive stress. Second, enlargement of the top capacitor plate enabled it to act as a structural bridge, preventing collapse and improving dimensional stability. Third, an air-elimination channel was incorporated into the diaphragm, allowing trapped air to escape during bonding and equalizing the internal and external pressures. To validate their effectiveness, four fabrication groups were studied, each incorporating a different combination of strategies. Group 1 (enlarged plate & air-elimination channel) exhibited coil deformation of  $11.7 \pm 4.3$  µm and a minor outward diaphragm deformation (approximately 1 µm) due to residual thermal stress from gold e-beam deposition (Fig. S4). Group 2 (open window & air-elimination channel) reduced coil deformation to  $3.1 \pm 0.5$  µm, although diaphragm deformation persisted at approximately 1 µm. In this case, the absence of a supporting plate allowed localized collapse of the softened SU-8 during bonding (Fig. S5). Group 3 (open window & enlarged plate) displayed outward coil deformation (approximately 3 µm), but severe diaphragm collapse of  $10.9 \pm 9.4$  µm due to trapped air (Fig. S6). Finally, Group 4 (full optimization: open window & enlarged plate & air-elimination channel) achieved excellent flatness, with minimal coil ( $\sim 3.8 \pm 0.3$  µm outward) and diaphragm (approximately 1 µm) deformation (Fig. 2b–e). Despite the success of Group 4, a small residual coil deformation (approximately 3 µm) was still detected, which was attributed to the spin-coating of photoresist

after electroplating. This additional thickness increased structural unevenness, creating bonding irregularities. To resolve this issue, the coil was released from the wafer and bonded using the original wafer contact surface, followed by PDMS-assisted lamination under external pressure to ensure complete sealing (Figs. S7, S8).

The electrical characteristics of the four sensor groups were systematically evaluated using a vector network analyzer (VNA), which enables precise monitoring of resonance frequency shifts in response to applied pressure stimuli. The optimized group (Group 4) exhibited the most reliable and reproducible performance, with a baseline resonance frequency of  $82.73 \pm 1.72$  MHz and a frequency fluctuation of only 2.1% across devices (Fig. 2f, g). This high degree of stability is essential for dual-sensor FFR applications, where accurate comparison between proximal and distal pressures requires nearly identical baseline resonance values. In addition to frequency stability, Group 4 demonstrated consistent pressure sensitivity of  $37.5 \pm 2.1$  kHz·mmHg<sup>-1</sup>, with a variability of just 5.7% (Fig. 2h). This performance confirms that the optimization strategies not only reduced structural deformation but also enhanced transduction efficiency and device reproducibility.

By contrast, sensors fabricated without optimization display higher apparent sensitivity. This effect was largely attributed to the reduced gap between capacitor plates caused by severe deformation during bonding. Although this smaller gap amplified capacitance changes in response to applied pressure, the corresponding resonance frequencies exhibited substantial drift and instability. As a result, the unoptimized devices produced inconsistent outputs that are unsuitable for longitudinal hemodynamic monitoring. Importantly, the instability of these devices underscores the trade-off between responsiveness and reliability: while high raw sensitivity may appear advantageous, without baseline stability and reproducibility, it cannot support clinically meaningful pressure measurements. These results demonstrate the fully optimized process not only minimized structural deformation but also established the performance stability required for accurate FFR monitoring in a dual-sensor smart stent platform.

The structural features of the fabricated LC-based wireless pressure sensor were examined in detail using scanning electron microscopy (SEM). Figure 3a shows the electroplated capacitor plate with a diameter of 16.1 mm. Notably, the plate diameter exceeds that of the underlying cavity (13 mm), allowing it to span the opening and act as a structural bridge. This design choice is critical because it prevents sagging or collapse of the SU-8 layer under elevated bonding temperatures, thereby maintaining capacitor alignment and stability. A magnified view of the inductor coil highlights the precisely

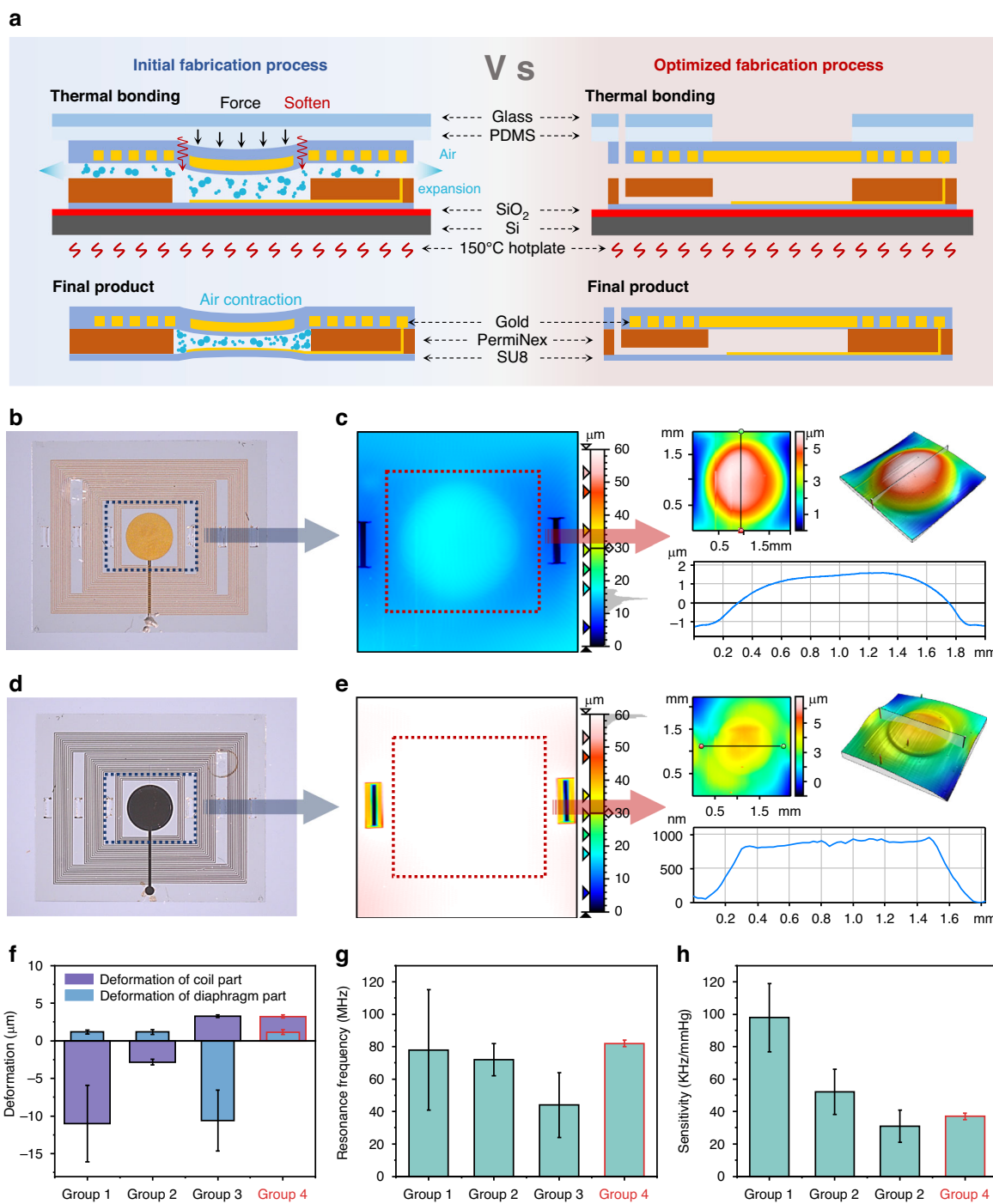
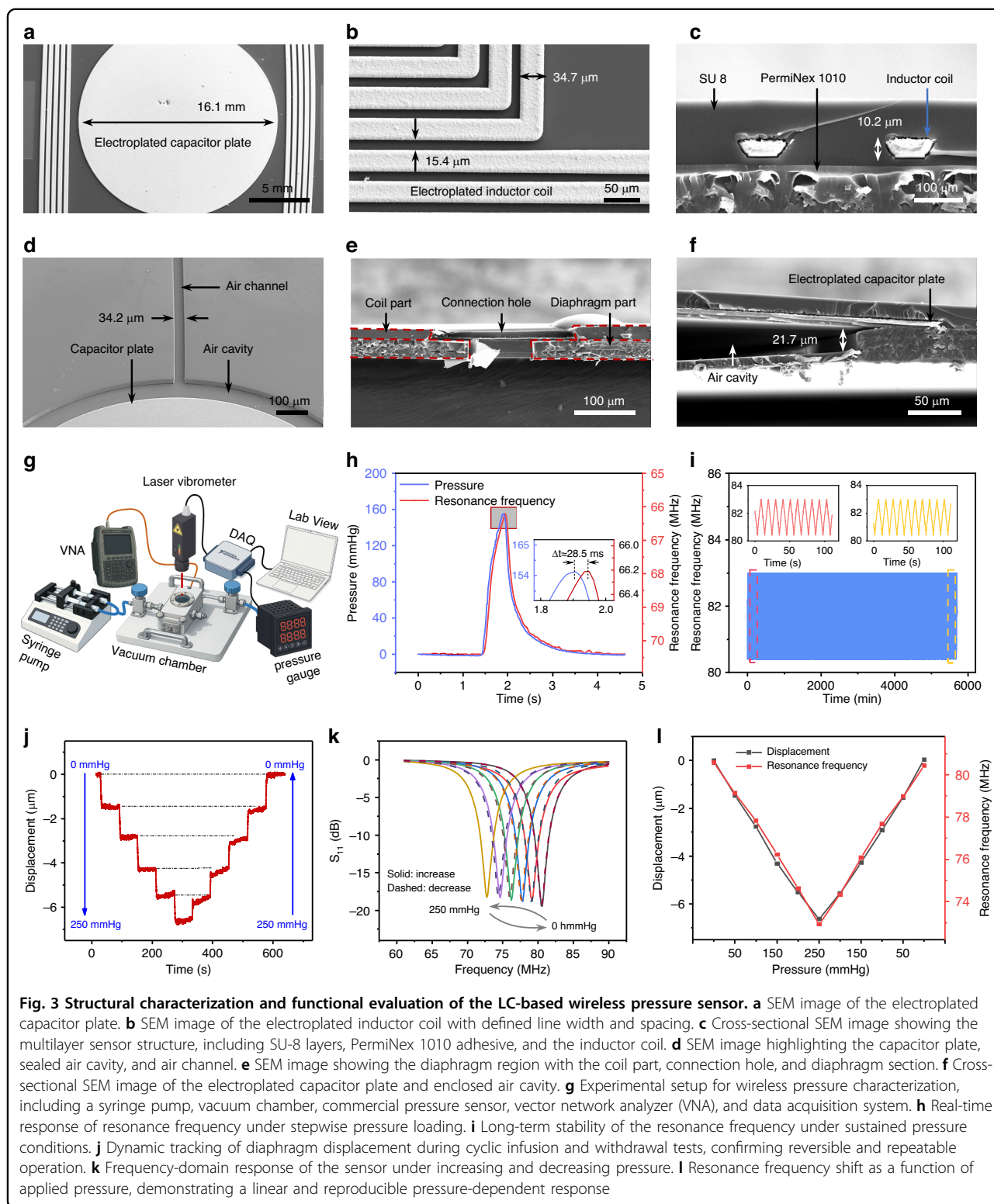


**Fig. 2 Comparison of conventional and optimized fabrication of LC pressure sensors.** **a** Schematic illustration of the conventional thermal bonding process and the optimized fabrication strategy, highlighting reduced structural deformation. **b, d** Optical micrographs of the diaphragm and coil structures fabricated using conventional and optimized processes. **c, e** Surface profilometry maps and corresponding line profiles of the diaphragm regions, showing pronounced deflection in the conventional process and minimal displacement in the optimized process. **f** Quantitative analysis of diaphragm and coil deformation across four fabrication groups, demonstrating significant suppression of structural distortion in Group 4 (optimized). **g, h** Measured resonance frequency variation and sensitivity across Groups 1-4, indicating improved baseline frequency stability and consistent sensor performance with the optimized process



defined electroplated copper traces, with a line width of 34.7 μm and spacing of 15.4 μm (Fig. 3b). The uniformity of these patterns confirms the high fidelity of the combined photolithography and electroplating processes,

which are essential for ensuring consistent inductance values across batches.

Cross-sectional SEM imaging reveals the multilayer configuration of the device, comprising SU-8 as the

structural framework, PermiNex 1010 as the bonding adhesive, and the embedded inductor coil with a measured thickness of approximately  $10.2\ \mu\text{m}$  (Fig. 3c). The diaphragm region is presented in Fig. 3d–e. The cavity provides the mechanical compliance necessary for diaphragm deflection under applied pressure, enabling capacitive modulation of the LC circuit. A venting microchannel with a diameter of approximately  $34.2\ \mu\text{m}$  was intentionally integrated into the diaphragm to equalize pressure during thermal bonding (Fig. 3d). By allowing trapped air to escape, this channel prevents undesired diaphragm collapse and improves reproducibility across devices. After thermal bonding, the coil and diaphragm components are integrated into a complete sensor. In addition, the presence of connection holes and diaphragm features ensures robust electrical and mechanical coupling between the coil and capacitor (Fig. 3e).

The resulting through-via, formed due to the size difference between connection holes in the two parts, can be filled with molten PCL during assembly, enabling stable attachment of the sensor to the polymer stent. Figure 3f further illustrates the electroplated capacitor plate suspended above a  $21.7\ \mu\text{m}$  air cavity, confirming successful cavity formation and mechanical integrity. The plate is seen bridging the cavity edges, acting simultaneously as a sensing electrode and a load-bearing support structure. Supplementary Fig. S9 provides additional evidence of electroplated thickness uniformity and compares the theoretical and measured inductance, showing excellent agreement. To evaluate device performance, a wireless characterization setup was constructed, as shown in Fig. 3g. A closed-loop pressure-control system was developed using a syringe pump coupled with a vacuum chamber, allowing precise modulation of internal pressure. A commercial pressure sensor monitored reference pressures in real time, while a laser vibrometer quantified membrane displacement. Simultaneously, a readout antenna placed near the device captured resonance frequency shifts, which were measured using a VNA. Rapid transient pressure changes were introduced by manually actuating the syringe, and synchronized resonance frequency responses were recorded via a LabVIEW interface. From these time-aligned datasets, the response time of the device was calculated to be  $20.8\ \text{ms}$  (Fig. 3h), which is sufficiently fast for capturing dynamic vascular pressure fluctuations.

To assess long-term operational stability, we evaluated the sensor performance under two representative conditions. First, under ambient laboratory conditions in air, a syringe pump was programmed to generate repeated infusion–withdrawal pressure cycles over a period of 100 h. Throughout this benchtop test, the resonance frequency response remained highly consistent with no

detectable signal degradation (Fig. 3i), confirming stable operation in a non-ionic environment. Second, to simulate physiological conditions, the device was immersed in PBS (pH 7.4) and maintained at  $37^\circ\text{C}$  for more than 100 h, during which the resonance frequency was continuously monitored oscillations throughout the test (Fig. S10). Additional electro-mechanical stability tests confirmed that the encapsulated SU-8/Au sensing module retained structural and chemical integrity during hydrolytic aging, and full datasets including radial force, SEM, and XPS analyses are provided in the Supporting Information (Figs. S11, S12, S13). A complementary study was conducted to examine how physiological environments affect the resonance characteristics of the wireless LC sensor. As detailed in the Supporting Information, immersion in saline causes a predictable downward shift in resonance frequency and a moderate reduction in Q-factor due to dielectric loading. Despite these changes, the sensor retains distinct resonance peaks and reliable pressure-dependent frequency shifts, confirming stable wireless operation under conditions comparable to blood (Fig. S14). Together, these findings demonstrate that the proposed device maintains excellent long-term stability and durability in both air and physiologically relevant ionic environments, supporting its suitability for extended implantation and continuous hemodynamic monitoring. Pressure cycling tests from 0 to 250 mmHg, applied in 50 mmHg increments, further demonstrated the sensor's repeatability and reversibility. The diaphragm exhibited maximum displacement of  $6.7\ \mu\text{m}$  at 250 mmHg, and reliably returned to baseline upon pressure release, indicating strong mechanical resilience (Fig. 3j). Corresponding resonance frequencies decreased with increasing pressure due to higher capacitance and returned to baseline with pressure release. Importantly, frequency responses were nearly identical during both pressurization and depressurization cycles, confirming negligible hysteresis (Fig. 3k). Figure 3l presents the fitted correlation between applied pressure, diaphragm displacement, and resonance frequency. The linear relationship across the full pressure range confirms reliable mechanical-to-electrical transduction.

Additional experiments were conducted to evaluate the robustness of wireless signal transmission between the implanted LC pressure sensor and the external antenna under various misalignment conditions, as shown in Fig. S15. Three alignment scenarios were investigated: vertical displacement, lateral offset, and angular rotation. In the vertical displacement test, the antenna was moved incrementally away from the sensor along the vertical axis (Fig. S15a). The  $S_{11}$  signal amplitude decreased with increasing distance, as expected due to reduced coupling efficiency. Nevertheless, even at a 10 mm separation, the resonance frequency shifts remained clearly detectable and

synchronized with the reference pressure waveform. In the lateral misalignment analysis, the antenna was displaced horizontally relative to the sensor (Fig. S15b). As the lateral offset increased, the  $S_{11}$  magnitude gradually declined, indicating weaker coupling. However, resonance frequency responses continued to track reference pressure signals with high fidelity up to 6 mm of lateral displacement. It is worth noting that this lateral displacement threshold is significantly smaller than the physical spacing between the two LC resonators integrated within the smart stent ( $\sim 10$  mm). Since detectable signals diminish before this separation distance, mutual coupling between the two resonators is inherently minimized, thereby preventing resonance frequency collision or interference during dual-sensor operation (Fig. S16). In the angular misalignment study, the antenna was rotated relative to the sensor while keeping the distance constant, producing an angular offset (Fig. S15c). Signal strength progressively decreased as the rotation angle increased, reflecting reduced mutual inductive coupling. Despite this, resonance frequency tracking of pressure cycles remained robust, even at rotation angles up to  $80^\circ$ . The ability of the sensor to maintain accurate frequency shifts under extreme angular misalignment highlights the resilience of the wireless coupling mechanism. Taken together, these results confirm that the LC-based wireless pressure sensor exhibits strong tolerance to positional variations of the external antenna, including vertical displacement, lateral offset, and angular rotation. The demonstrated stability of resonance frequency tracking under non-ideal conditions underscores the practical feasibility of continuous hemodynamic monitoring using the proposed smart stent system.

The vascular stent was fabricated using extrusion-based 3D printing, which allowed precise control over geometry and material distribution. The stent design was created in Aspire software and incorporated two distinct polymer components: PLA for the curved ring segments and PCL for the connecting struts (Fig. 4a). PLA is widely regarded as an ideal polymer for stent fabrication due to its excellent degradation characteristics and relatively high mechanical strength. Three-point bending tests performed according to ASTM F2606-08 (2021) confirmed that the pure PLA stent exhibited a radial force of  $0.1611 \text{ N mm}^{-1}$ , a value that meets clinical requirements for vascular stents. However, PLA's high melting temperature range ( $180\text{--}220^\circ\text{C}$ ) presents challenges for direct bonding with MEMS-based wireless pressure sensors. PCL, in contrast, has a much lower melting temperature of approximately  $60^\circ\text{C}$ , enabling facile bonding and thermal integration of electronic components. Nevertheless, pure PCL stents demonstrated insufficient mechanical performance, with a measured radial force of only  $0.0310 \text{ N mm}^{-1}$ , making them too soft to provide

adequate luminal support. To overcome the limitations of each individual material, a hybrid design was implemented in which PLA was used for the curve rings to provide radial strength, while PCL served as the connectors to impart flexibility and facilitate low-temperature bonding (Fig. 4b). The hybrid PLA/PCL stent delivered a radial force of  $0.1504 \text{ N mm}^{-1}$ , closely comparable to the pure PLA stent, while retaining the advantages of PCL for sensor bonding (Fig. 4c). This dual-material strategy thus ensures both mechanical compliance and integration compatibility, which are essential for fabricating a robust yet functional smart stent.

A major challenge in developing a clinically deployable smart stent lies in sensor integration. Conventional strategies typically attach the pressure sensor to the inner stent wall before crimping. However, this internal placement exposes the device to extreme bending strain during expansion, often leading to mechanical damage, delamination, or functional failure (Fig. S17). To address this issue, a modified strategy was developed. The stent was first mechanically crimped from its original diameter of 4 mm to 2 mm using a custom jig. The wireless pressure sensor was then externally mounted onto the crimped stent, avoiding exposure to high radial compression. Pre-designed connection holes on the sensor were aligned with the PCL struts and thermally fused using molten PCL to achieve strong adhesion. To ensure conformal attachment, the partially integrated sensor–stent assembly was placed into a circular mold, and a thin layer of biocompatible, water-soluble PVA was applied to maintain intimate contact during curing (Fig. 4d). The fully assembled smart stent was then mounted on a balloon catheter for delivery. Successful expansion and vascular apposition were demonstrated in a transparent tubing model (Fig. 4e) and within the 3 mm-diameter coronary artery regions of a heart phantom (Fig. 4f). In both cases, the device expanded uniformly at an inflation pressure of 1.8 atm and maintained stable apposition to the vessel wall, confirming compatibility with clinical catheter-based procedures.

Functional validation was performed in a closed-loop phantom system designed to replicate physiologically relevant pulsatile pressure conditions. The setup incorporated a pulse pump to generate controlled pulsatile flow, a commercial pressure transducer as the reference standard, and a VNA for wireless interrogation of the implanted LC sensor. Resonance frequency traces were sampled at 20 Hz over 10 s intervals, providing sufficient temporal resolution to capture rapid hemodynamic fluctuations (Fig. 4g). The raw  $S_{11}$  spectra revealed clear pressure-induced shifts of the resonance frequency, ranging from approximately 38.1 to 38.6 MHz during the pulsatile cycles. To enhance data reliability, the time series was processed using a custom Python algorithm that

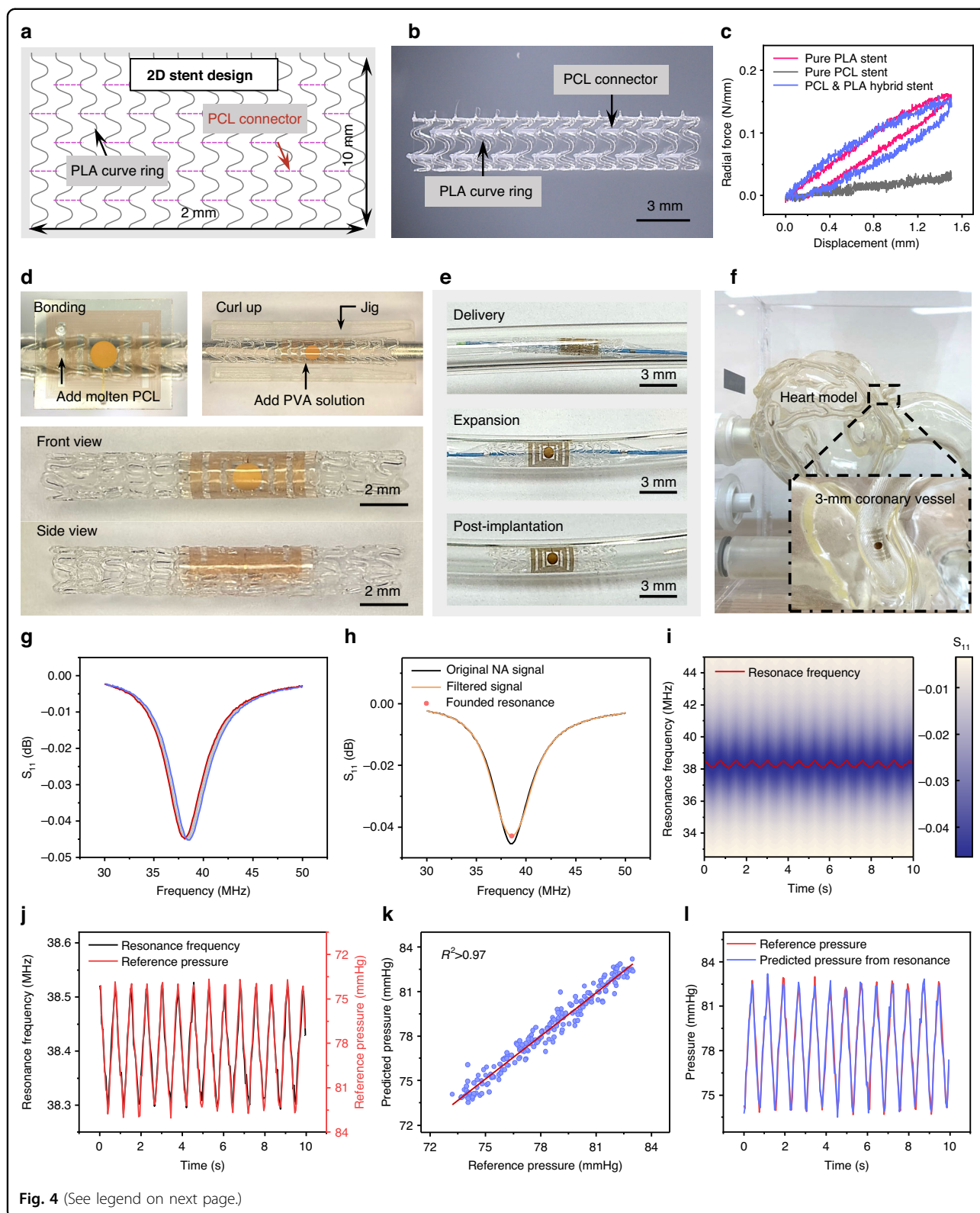


**Fig. 4** (See legend on next page.)

applied smoothing and automated detection of resonance minima (Fig. 4h). This processing enabled accurate extraction of resonance features while minimizing noise

and baseline drift. The temporal evolution of the resonance was visualized as an  $S_{11}$  spectrogram (Fig. 4i), which clearly illustrated the dynamic response of the

(see figure on previous page)

**Fig. 4 Fabrication, integration, deployment, and functional validation of the smart stent system.** **a** Two-dimensional design of the hybrid polymer stent incorporating PLA curve rings and PCL connectors. **b** Optical image of the 3D-printed stent fabricated from PCL/PLA hybrid material. **c** Radial force comparison of stents composed of pure PCL, pure PLA, and hybrid PCL/PLA, demonstrating enhanced mechanical strength of the hybrid structure. **d** Optical images of the wireless pressure sensor and stent prior to and following integration using a PVA-based coupling layer. **e** Stepwise catheter-based delivery process showing crimping, expansion, and vascular apposition of the smart stent. **f** Deployment of the integrated device into a 3 mm-diameter coronary artery phantom, confirming compatibility with standard balloon-catheter procedures. **g** Resonance frequency response recorded under varying hydrostatic pressures, simulating physiological hemodynamic conditions. **h, i** Extraction of resonance frequency minima and curve fitting, highlighting pressure-dependent frequency shifts. **j** Correlation between applied pressure and resonance frequency derived from fitted data. **k** Linear regression analysis confirming strong agreement between applied pressure and frequency response. **l** Comparison of predicted versus measured pressure values, validating the reliability of the smart stent for real-time intravascular pressure monitoring

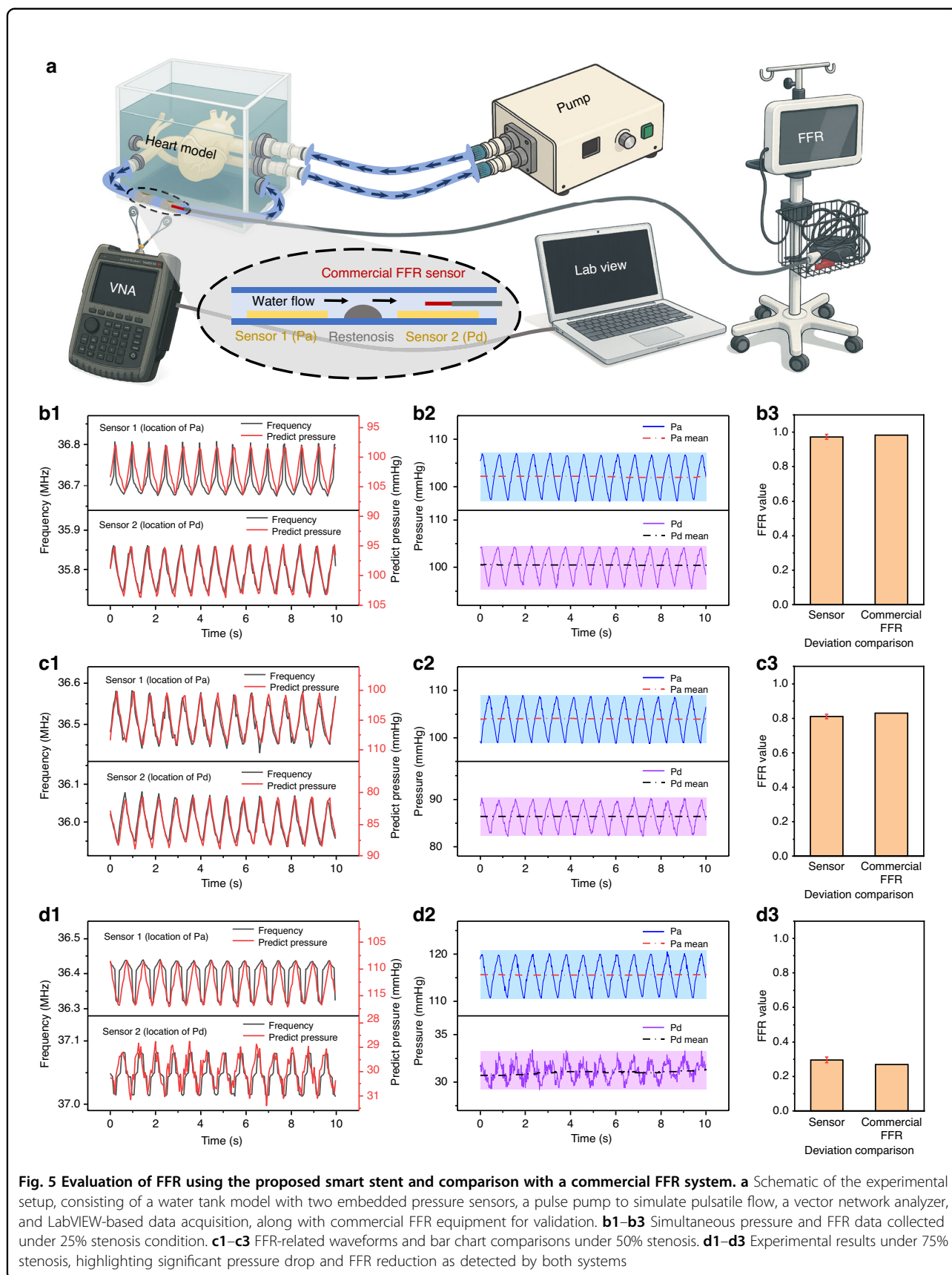
wireless sensor to repeated pressure fluctuations. The resonance frequency response closely tracked the imposed pulsatile waveform, with frequency shifts that scaled linearly with applied pressure (Fig. 4j). Linear regression analysis against the commercial pressure transducer confirmed excellent agreement, yielding a coefficient of determination of  $R^2 = 0.97$  (Fig. 4k). To further assess the agreement between the two measurement methods beyond linear correlation, a Bland–Altman analysis was performed. As shown in Fig. S18, the mean bias between the reference transducer and the wireless sensor was close to zero, and the limits of agreement remained well within  $\pm 1.0$  mmHg, indicating no systematic overestimation or underestimation by the proposed device. The narrow dispersion of data points around the zero line confirms that the reconstructed pressures are statistically interchangeable with those of the commercial sensor and validates the clinical relevance of the wireless readout. Based on this calibration, the wireless resonance signals were converted into reconstructed pressure values. The predicted waveform showed nearly perfect overlap with the reference signal, validating the accuracy, stability, and reproducibility of the wireless sensing mechanism (Fig. 4l).

Collectively, these results demonstrate that the smart stent is capable of faithfully capturing dynamic intraluminal pressure changes in real time, translating mechanical pulsations into precise electrical readouts. Comprehensive characterization of the readout performance is provided in the Supporting Information. This includes frequency noise analysis and limit-of-detection calculations based on resonance fluctuations under zero pressure (Fig. S19), as well as small-step pressure discrimination studies that report signal-to-noise ratio (SNR), area-under-the-curve (AUC), and 100% detection hit rate for pressure increments down to 1 mmHg (Fig. S20). Thermal drift measurements and long-term resonance tracking further confirm that physiological temperature variations (34–40 °C) induce only minor frequency shifts that do not compromise sensing accuracy (Fig. S21). Likewise, pH-dependent testing in PBS solutions (pH 6.8–7.8) shows negligible changes in baseline resonance, sensitivity, or detection limit, validating sensor

robustness in chemically relevant environments (Fig. S22). A depth-dependent wireless coupling analysis conducted in a saline phantom confirmed that the resonance signal remained clearly detectable over implantation depths up to 10 mm, with only modest attenuation and no loss of sensing capability (Fig. S23). Table S1 provides a concise summary of the key experimental conditions and sensing performance metrics, facilitating a direct and intuitive comparison across different experimental scenarios. Finally, hemocompatibility and cytotoxicity assays demonstrate that neither the hybrid stent nor the integrated wireless sensor elicits adverse biological responses, supporting their suitability for vascular implantation. Full datasets and experimental details are provided in the Supporting Information (Figs. S24, S25).

FFR is widely regarded as the clinical gold standard for evaluating the physiological significance of coronary stenosis, as it directly reflects the impact of luminal narrowing on downstream blood flow. In this study, we implemented a dual-sensor configuration within the hybrid BVS to enable simultaneous measurement of proximal (Pa) and distal (Pd) pressures, allowing real-time calculation of FFR as the ratio Pd/Pa. The experimental setup is illustrated in Fig. 5a, consisting of a water tank and tubing phantom with pulsatile flow generated by a pulse pump, a VNA for wireless data acquisition, a LabVIEW interface for signal processing, and a commercial FFR system for validation. Obstruction blocks were inserted into the tubing to mimic varying stenosis severities (0%, 25%, 50%, and 75%). A 3-mm-diameter stent model was designed in SolidWorks, with the mid-segment lumen partially occluded to replicate 25%, 50%, and 75% diameter restenosis conditions. The models were fabricated using a high-precision 3D printer with a resolution of 35  $\mu\text{m}$ . Two wireless pressure sensors were bonded with resin at the proximal (Pa) and distal (Pd) ends of the stenotic segment to enable simultaneous pressure measurements. For comparison, a commercial FFR pressure sensor was advanced through a guide catheter and positioned co-axially with the smart stent to record Pa and Pd at the same anatomical sites.

The resonance frequency shifts from each sensor were recorded and converted into pressure values, enabling



calculation of FFR values for direct comparison with the commercial system. Under the baseline (0% stenosis) condition, Pa and Pd were nearly identical, yielding an FFR of  $0.973 \pm 0.012$  from the wireless system and  $0.998 \pm 0.007$  from the commercial probe (Fig. 5b1–b3). At 25% stenosis, Pd decreased by 3 mmHg relative to Pa, and the calculated FFR values were  $0.963 \pm 0.014$  (wireless) and  $0.983 \pm 0.008$  (commercial), showing excellent agreement. With further stenosis progression to 50%, a more pronounced gradient developed, with Pa increasing by 2 mmHg and Pd decreasing by 14 mmHg.

The resulting FFR values were  $0.811 \pm 0.012$  and  $0.831 \pm 0.008$  for the wireless and commercial systems, respectively (Fig. 5c1–c3). Finally, under severe stenosis (75%), flow was markedly restricted, and the pressure gradient was substantial (Pa increased by 14 mmHg, Pd dropped by 69 mmHg). The smart stent measured an FFR of  $0.296 \pm 0.017$  compared with  $0.268 \pm 0.009$  from the commercial system (Fig. 5d1–d3). The maximum deviation of 0.028 between the two systems was attributed to reduced signal amplitude and increased noise at the low Pd site, yet the values remained within clinically acceptable limits. These results demonstrate that the smart stent not only tracks pressure variations with high fidelity but also provides FFR values closely matching those of an established commercial system across a broad range of stenosis severities. The ability to obtain such accurate measurements using a fully implantable, wireless, and bioresorbable device represents a major advancement over conventional catheter-based approaches, which are invasive, intermittent, and limited to acute measurements. The proposed dual-sensor smart stent thus establishes a minimally invasive platform for continuous and long-term monitoring of vascular physiology. By enabling real-time detection of subtle pressure differentials and early reductions in FFR, this technology holds strong potential for improving the management of in-stent restenosis and guiding timely clinical intervention. Although the present platform employs a biostable MEMS-based wireless sensor integrated on a bioresorbable stent, the system architecture is inherently compatible with future adoption of transient electronic components. Emerging biodegradable conductors such as Mg, Zn, and Mo, together with dissolvable dielectric and encapsulation materials, provide a credible materials pathway for the realization of fully resorbable pressure-sensing modules. Nevertheless, challenges remain in achieving controlled corrosion kinetics, preserving electrical performance during degradation, and ensuring long-term signal fidelity. Addressing these aspects constitutes an important direction for translating this work toward next-generation, fully bioresorbable smart stent systems.

## Conclusion

In this study, we developed and validated a wireless LC-based pressure sensing system integrated with a bioresorbable polymer stent for real-time vascular monitoring. The MEMS-fabricated pressure sensor exhibited excellent structural integrity, mechanical resilience, and high sensitivity. Key design optimizations, including refinement of the diaphragm geometry and improvements in thermal bonding, minimized deformation and enhanced fabrication reliability. The resulting sensor demonstrated a baseline resonance frequency of  $82.2 \pm 1.7$  MHz and a pressure sensitivity of  $37.48 \pm 2.13$  kHz/mmHg, along with rapid response dynamics and long-term operational stability. To construct a catheter-deployable smart stent system, a hybrid BVS composed of PLA and PCL was fabricated using extrusion-based 3D printing. The wireless pressure sensor was externally mounted onto the pre-crimped stent using thermally bonded PCL, thereby preventing structural damage during catheter delivery. The assembled smart stent was deployed into a vascular phantom using a balloon catheter and demonstrated reliable pressure sensing under pulsatile flow conditions. Resonance frequency data collected during simulated blood pressure cycles were processed using a Python-based algorithm, enabling accurate reconstruction of real-time pressure waveforms with excellent agreement ( $R^2 = 0.97$ ) compared to commercial pressure sensors. Beyond single-point monitoring, a dual-sensor configuration enabled real-time assessment of FFR. Under simulated stenosis conditions ranging from 0% to 75%, the smart stent system accurately captured pressure differentials between upstream and downstream locations. The FFR values derived from the wireless sensors closely matched those obtained with a commercial FFR system, with minimal deviation across all severity levels, confirming the diagnostic reliability of the platform. Collectively, this work demonstrates a fully integrated, wireless, and catheter-deployable smart stent system capable of real-time pressure monitoring and FFR measurement. This approach offers significant potential for early diagnosis and management of vascular diseases through minimally invasive intervention. Future work will focus on validating the system in physiologically relevant environments. Ex vivo experiments using perfused porcine or bovine arteries will be conducted to benchmark the wireless FFR measurements against those obtained from a commercial FFR wire under pulsatile flow conditions. Following successful ex vivo verification, large-animal in vivo studies will be undertaken to assess long-term mechanical performance, biodegradation behavior, inflammatory response, and continuous pressure monitoring.

## Materials and methods

### Materials

Silicon wafers were obtained from Silicon Technology Cooperation (Korea). SU-8 3010, SU8-6002 and PermiNex 1000 were sourced from Kayaku Advanced Materials. The photosensitive resist AZ4620 and buffered oxide etchant (BHF) were purchased from MicroChemicals (Germany). Polycaprolactone (PCL, Mw 80,000), Polylactic Acid (PLA, Mw 260,000) were obtained from Sigma-Aldrich. Polyvinyl alcohol (PVA, Mw 6000) was purchased from Polysciences (UK). Conductive epoxy was purchased from CHEMTRONICS (USA).

### Fabrication of LC wireless pressure sensors

The detailed fabrication process is schematically illustrated in Figure S26. The fabrication begins by oxidizing a silicon wafer at 1000 °C for 38 min to grow a 300 nm SiO<sub>2</sub> sacrificial layer. The coil part is fabricated by patterning a 2 μm SU8-2002 base layer on the oxide surface. A Ti/Au (10 nm/200 nm) metal layer was then deposited via electron-beam evaporation to serve as seed layer. A 12 μm AZ 4620 photoresist layer is subsequently patterned through photolithography to define the 32-turn inductor and the 1.5 mm-diameter capacitor plate. Au electroplating, followed by metal etching to remove the redundant seed layer, increases the thickness of these structures to approximately 10 μm. All that structure is encapsulated with SU8-3010, and additional photolithography steps are used to open the air elimination hole and mechanical connection hole. The complete coil part is released by etching the sacrificial layer in BHF solution. For the diaphragm part, a 10 μm SU8-3010 base is patterned, followed by Ti/Au metal deposition under the same parameters used for the coil. GXR photoresist is used to define the capacitor plate shape, and selective Ti/Au wet etching removes exposed areas. PermiNex 1010 is then patterned to define a cavity of 1.2 mm diameter and 20 μm depth, along with a 50 μm-wide air elimination channel. Due to the diameter mismatch between the cavity and the capacitor plate located in the coil part, the structure extends over the cavity to form a suspended supporting bridge. This suspended design prevents deformation during bonding, even at elevated temperatures where SU-8 is softening. The proposed air-elimination channel is designed to prevent pressure-induced deformation from trapped air during bonding, extending from the cavity to an air-elimination hole on the coil region. This dual opening mechanism allows the internal air to expand and escape during heating and bonding, then re-enter upon cooling to equalize internal and external pressures. The coil and diaphragm parts are then aligned manually under a microscope, placed on a 150 °C hot plate, and thermally bonded using the

PermiNex photoresist layer. A PDMS and slide-glass based press block with air elimination hole and open window, prepared by spin-coating and laser etching, is used to apply uniform pressure during bonding. During bonding, the open-window structure above the capacitor plate prevents vertical pressure from causing uncontrolled deformation of the sensing elements. This design effectively reduces the mechanical load on the capacitor plate, particularly during hot-pressing at 150 °C, thereby preserving the structural integrity of the LC resonant circuit and ensuring consistent sensor performance. After bonding and cooling, conductive epoxy is applied to electrically connect the coil and diaphragm. The air elimination hole is sealed using epoxy resin. Finally, the device is released from the wafer by BHF etching of the SiO<sub>2</sub> sacrificial layer, resulting in the fully assembled wireless pressure sensor.

### Fabrication of PCL/PLA hybrid stent

The stent was fabricated using a dual-nozzle, extrusion-based 3D printer with four degrees of freedom (spindle rotation, Y-axis translation of the spindle base, and X-/Z-axis movement of the nozzles) for precise spatial control. The geometry of the stent is designed in Aspire CAD software, followed a conventional architecture of wavy circular rings interconnected by straight struts. PLA was used for wavy rings to provide high rigidity, while PCL was used for the struts to enhance flexibility. A stainless-steel shaft coated with a water-soluble PVA layer served as the printing substrate, enabling easy release after fabrication. During the printing process, PCL was extruded first due to its lower melting point, followed by PLA extrusion along the predefined paths. At locations where the two materials intersect, heat transfer from the PLA nozzle induced localized melting of both materials, promoting interfacial bonding and structural integration. The composite printing strategy ensured mechanical synergy between the rigid PLA rings and the flexible PCL struts, forming a functionally graded hybrid stent. After printing, the assembled PCL/PLA hybrid BVS and the supporting metal shaft were immersed in DI water to dissolve the PVA sacrificial layer.

### Fabrication of smart stent

To fabricate the smart stent, a plastic shaft was inserted into the previously prepared PCL/PLA hybrid BVS to define its minimum internal diameter during the crimping process. The stent, along with the shaft, was placed into a crimping machine and subjected to a temperature of 40 °C and a pressure of 2 atm. This process reduced the stent diameter to 2 mm, making it suitable for intravascular delivery. The LC wireless pressure sensor was then aligned under a microscope with the strut region of the

stent. The connection hole on the sensor was positioned to match the PCL section of the hybrid stent. PCL pellets were applied to the aligned region and heated under pressure, allowing the melted PCL to flow into the connection hole and fuse the sensor to the stent. Upon cooling, a mechanically stable integration was achieved between the sensor and the PCL structure. After the initial attachment, the sensor-stent assembly was placed into a specially designed fixture. This fixture ensured that the sensor conformed closely to the curvature of the stent during setting. A 30 wt% aqueous PVA solution was applied at the interface. Once solidified, the PVA layer held the sensor and stent in tight contact during handling. Following fixture removal, the final smart stent with a compressed diameter of 2 mm was obtained. This device is compatible with standard balloon catheter-based deployment and enables wireless pressure sensing through the integrated LC sensor.

#### Acknowledgements

This work was supported by the National Research Foundation of Korea (NRF) grant funded by the Korea government (MSIT) (No. RS-2020-NR049568 and RS-2022-00165505). All the authors sincerely appreciate the considerable help received from Mr. Ashfaq Ahmad and Prof. Hee-Gyeong Yi during this investigation.

#### Author details

<sup>1</sup>MEMS and Nanotechnology Laboratory, School of Mechanical Engineering, Chonnam National University, Gwangju, Republic of Korea. <sup>2</sup>Advanced Medical Device Research Center for Cardiovascular Disease, Chonnam National University, Gwangju, Republic of Korea. <sup>3</sup>Center for Next-Generation Sensor Research and Development, Chonnam National University, Gwangju, Republic of Korea

#### Author contributions

J.W. designed and performed all experiments and was the primary contributor to manuscript preparation. A.S. assisted with data analysis, interpretation, and manuscript writing, review, and editing. N.-M.O. contributed to data analysis and interpretation. L.W. contributed to data analysis and interpretation. As corresponding author, D.-W.L. supervised the project and provided critical guidance as well as substantive revisions to the manuscript. All authors reviewed and approved the final version of the manuscript.

#### Conflict of interest

The authors declare no competing interests.

**Supplementary information** The online version contains supplementary material available at <https://doi.org/10.1038/s41378-026-01182-8>.

Received: 16 September 2025 Revised: 1 January 2026 Accepted: 6 January 2026

Published online: 31 March 2026

#### References

- Federation, W. H. *Deaths from cardiovascular disease surged 60% globally over the last 30 years: Report* <https://world-heart-federation.org/news/deaths-from-cardiovascular-disease-surged-60-globally-over-the-last-30-years-report/> (2023).
- Chong, B. et al. Global burden of cardiovascular diseases: projections from 2025 to 2050. *Eur. J. Prev. Cardiol.* **32**, 1001–1015, <https://doi.org/10.1093/eurjpc/zwae281> (2025).
- Tsao, C. W. et al. Heart disease and stroke statistics—2022 Update: A Report From the American Heart Association. *Circulation* **145** (2022). <https://doi.org/10.1161/cir.0000000000001052>
- Association, A. H. *Population shifts, risk factors may triple U.S. cardiovascular disease costs by 2050* <https://newsroom.heart.org/news/population-shifts-risk-factors-may-triple-u-s-cardiovascular-disease-costs-by-2050> (2024).
- Libby, P. et al. Atherosclerosis. *Nat. Rev. Dis. Primers* **5** (2019). <https://doi.org/10.1038/s41572-019-0106-z>
- Björkegren, J. L. M. & Lusis, A. J. Atherosclerosis: recent developments. *Cell* **185**, 1630–1645, <https://doi.org/10.1016/j.cell.2022.04.004> (2022).
- Bentzon, J. F., Otsuka, F., Virmani, R. & Falk, E. Mechanisms of plaque formation and rupture. *Circ. Res.* **114**, 1852–1866, <https://doi.org/10.1161/circresaha.114.302721> (2014).
- Młynarska, E. et al. From Atherosclerotic plaque to myocardial infarction—the leading cause of coronary artery occlusion. *Int. J. Mol. Sci.* **25** (2024). <https://doi.org/10.3390/ijms25137295>
- Boden, W. E. et al. Optimal medical therapy with or without pci for stable coronary disease. *N. Engl. J. Med.* **356**, 1503–1516, <https://doi.org/10.1056/NEJMoa070829> (2007).
- Lawton, J. S. et al. 2021 ACC/AHA/SCAI guideline for coronary artery revascularization: executive summary: A report of the american college of cardiology/american heart association joint committee on clinical practice guidelines. *Circulation* **145** (2022). <https://doi.org/10.1161/cir.0000000000001039>
- Buccheri, D., Piraino, D., Andolina, G. & Cortese, B. Understanding and managing in-stent restenosis: a review of clinical data, from pathogenesis to treatment. *J. Thorac. Dis.* **8**, E1150–E1162, <https://doi.org/10.21037/jtd.2016.10.93> (2016).
- Byrne, R. A., Joner, M. & Kastrati, A. Stent thrombosis and restenosis: what have we learned and where are we going? The Andreas Gruntzig Lecture ESC 2014. *Eur. Heart J.* **36**, 3320–3331, <https://doi.org/10.1093/eurheartj/ehv511> (2015).
- Kornowski, R. et al. In-stent restenosis: contributions of inflammatory responses and arterial injury to neointimal hyperplasia. *J. Am. Coll. Cardiol.* **31**, 224–230, [https://doi.org/10.1016/s0735-1097\(97\)00450-6](https://doi.org/10.1016/s0735-1097(97)00450-6) (1998).
- Lowe, H. C., Oesterle, S. N. & Khachigian, L. M. Coronary in-stent restenosis: current status and future strategies. *J. Am. Coll. Cardiol.* **39**, 183–193, [https://doi.org/10.1016/s0735-1097\(01\)01742-9](https://doi.org/10.1016/s0735-1097(01)01742-9) (2002).
- Alfonso, F., Byrne, R. A., Rivero, F. & Kastrati, A. Current treatment of in-stent restenosis. *J. Am. Coll. Cardiol.* **63**, 2659–2673, <https://doi.org/10.1016/j.jacc.2014.02.545> (2014).
- Borhani, S., Hassanajili, S., Ahmadi Tafti, S. H. & Rabbani, S. Cardiovascular stents: overview, evolution, and next generation. *Prog. Biomater.* **7**, 175–205, <https://doi.org/10.1007/s40204-018-0097-y> (2018).
- Giustino, G. et al. Coronary in-stent restenosis state-of-the-art review. *J. Am. Coll. Cardiol.* **80**, 348–372, <https://doi.org/10.1016/j.jacc.2022.05.017> (2022).
- Jinnouchi, H. et al. Fully bioresorbable vascular scaffolds: lessons learned and future directions. *Nat. Rev. Cardiol.* **16**, 286–304, <https://doi.org/10.1038/s41569-018-0124-7> (2019).
- Foin, N. et al. Bioabsorbable vascular scaffold overexpansion: insights from in vitro post-expansion experiments. *EuroIntervention* **11**, 1389–1399, [https://doi.org/10.4244/EIJY15M07\\_02](https://doi.org/10.4244/EIJY15M07_02) (2016).
- Toyota, T. et al. Very late scaffold thrombosis of bioresorbable vascular scaffold. *Syst. Rev. Meta-Anal. JACC Cardiovasc. Inter.* **10**, 27–37, <https://doi.org/10.1016/j.jcin.2016.10.027> (2017).
- Dangas, G. D. et al. In-stent restenosis in the drug-eluting stent era. *J. Am. Coll. Cardiol.* **56**, 1897–1907, <https://doi.org/10.1016/j.jacc.2010.07.028> (2010).
- Joner, M. et al. Pathology of drug-eluting stents in humans - Delayed healing and late thrombotic risk. *J. Am. Coll. Cardiol.* **48**, 193–202, <https://doi.org/10.1016/j.jacc.2006.03.042> (2006).
- Finn, A. V. et al. Pathological correlates of late drug-eluting stent thrombosis. *Circulation* **115**, 2435–2441, <https://doi.org/10.1161/circulationaha.107.693739> (2007).
- Waksman, R. et al. Correlates and outcomes of late and very late drug-eluting stent thrombosis. *JACC Cardiovasc. Interv.* **7**, 1093–1102, <https://doi.org/10.1016/j.jcin.2014.04.017> (2014).
- Mukheja, Y. et al. Unravelling the progress and potential of drug-eluting stents and drug-coated balloons in cardiologic insurgencies. *Life Sci.* **352** (2024). <https://doi.org/10.1016/j.lfs.2024.122908>
- Adriaenssens, T. et al. Optical coherence tomography findings in patients with coronary stent thrombosis. *Circulation* **136**, 1007–1021, <https://doi.org/10.1161/circulationaha.117.026788> (2017).

27. Shlofmitz, E. et al. Intravascular imaging-guided percutaneous coronary intervention. *Circ. Cardiovasc. Interv.* **13** (2020). <https://doi.org/10.1161/circinterventions.120.008686>
28. Mintz, G. S., Matsumura, M., Ali, Z. & Maehara, A. Clinical utility of intravascular imaging: past, present, and future. *JACC: Cardiovasc. Imaging* **15**, 1799–1820, <https://doi.org/10.1016/j.jcmg.2022.04.026> (2022).
29. Kang, D.-Y. et al. Optical coherence tomography-guided or intravascular ultrasound-guided percutaneous coronary intervention: The octivus randomized clinical trial. *Circulation* **148**, 1195–1206, <https://doi.org/10.1161/circulationaha.123.066429> (2023).
30. Koo, B.-K. et al. Fractional flow reserve or intravascular ultrasonography to guide PCI. *N. Engl. J. Med.* **387**, 779–789, <https://doi.org/10.1056/NEJMoa2201546> (2022).
31. Fearon, W. F. et al. Fractional flow reserve compared with intravascular ultrasound guidance for optimizing stent deployment. *Circulation* **104**, 1917–1922, <https://doi.org/10.1161/hc4f01.097539> (2001).
32. Cutlip, D. E. et al. Clinical restenosis after coronary stenting: Perspectives from multicenter clinical trials. *J. Am. Coll. Cardiol.* **40**, 2082–2089, [https://doi.org/10.1016/S0735-1097\(02\)02597-4](https://doi.org/10.1016/S0735-1097(02)02597-4) (2002).
33. Pijls, N. H. J. et al. Coronary pressure measurement after stenting predicts adverse events at follow-up—a multicenter registry. *Circulation* **105**, 2950–2954, <https://doi.org/10.1161/01.Cir.0000020547.92091.76> (2002).
34. Rivero, F. et al. Reliability of physiological assessment of coronary stenosis severity using intracoronary pressure techniques: a comprehensive analysis from a large cohort of consecutive intermediate coronary lesions. *Eurointervention* **13**, E193–E200, <https://doi.org/10.4244/Eij-D-16-00574> (2017).
35. Scarsini, R. et al. Functional patterns of coronary disease. *Diffus. Focal Ser. Lesions Jacc-Cardiovasc. Interv.* **15**, 2174–2191, <https://doi.org/10.1016/j.jcin.2022.07.015> (2022).
36. Piroth, Z. et al. Prognostic value of measuring fractional flow reserve after percutaneous coronary intervention in patients with complex coronary artery disease: insights from the fame 3 trial. *Circ. Cardiovasc. Interv.* **15**, 884–891, <https://doi.org/10.1161/circinterventions.122.012542> (2022).
37. Corcoran, D., Hennigan, B. & Berry, C. Fractional flow reserve: a clinical perspective. *Int. J. Cardiovasc. Imaging* **33**, 961–974, <https://doi.org/10.1007/s10554-017-1159-2> (2017).
38. Jeremias, A., Kirtane, A. J. & Stone, G. W. A test in context fractional flow reserve: accuracy, prognostic implications, and limitations. *J. Am. Coll. Cardiol.* **69**, 2748–2758, <https://doi.org/10.1016/j.jacc.2017.04.019> (2017).
39. Pijls, N. H. J. et al. Measurement of fractional flow reserve to assess the functional severity of coronary-artery stenoses. *N. Engl. J. Med.* **334**, 1703–1708, <https://doi.org/10.1056/nejm199606273342604> (1996).
40. Oyunbaatar, N.-E. et al. Implantable self-reporting stents for detecting in-stent restenosis and cardiac functional dynamics. *ACS Sens.* **8**, 4542–4553, <https://doi.org/10.1021/acssensors.3c01313> (2023).
41. Chen, X., Assadsangabi, B., Hsiang, Y. & Takahata, K. Enabling angioplasty-ready “smart” stents to detect in-stent restenosis and occlusion. *Adv. Sci.* **5** (2018). <https://doi.org/10.1002/advs.201700560>
42. Chen, X., Brox, D., Assadsangabi, B., Hsiang, Y. & Takahata, K. Intelligent telemetric stent for wireless monitoring of intravascular pressure and its testing. *Biomed. Microdevices* **16**, 745–759, <https://doi.org/10.1007/s10544-014-9879-8> (2014).
43. Herbert, R., Lim, H. R., Rigo, B. & Yeo, W.-H. Fully implantable wireless batteryless vascular electronics with printed soft sensors for multiplex sensing of hemodynamics. *Sci. Adv.* **8**, eabm1175. <https://doi.org/10.1126/sciadv.abm1175> (2022).
44. Wang, L. et al. The Polycraft polymer–metal hybrid smart stent system: The future of cardiovascular blood pressure management. *Adv. Funct. Mater.* **34** (2024). <https://doi.org/10.1002/adfm.202408022>
45. Wei, J. et al. Enhancing flexibility of smart bioresorbable vascular scaffolds through 3D printing using polycaprolactone and polylactic acid. *Sens. Actuat. B Chem.* **422** (2025). <https://doi.org/10.1016/j.snb.2024.136667>
46. Rich, A. M. et al. Development of an implantable sensor system for in vivo strain, temperature, and pH monitoring: comparative evaluation of titanium and resorbable magnesium plates. *Bioact. Mater.* **43**, 603–618, <https://doi.org/10.1016/j.bioactmat.2024.09.015> (2025).
47. Song, J. et al. Polyelectrolyte-based wireless and drift-free iontronic sensors for orthodontic sensing. *Sci. Adv.* **11** (2025). <https://doi.org/10.1126/sciadv.adu6086>
48. Casadonte, L., Piek, J. J., VanBavel, E., Spaan, J. A. E. & Siebes, M. Discordance between pressure drift after wire pullback and intracoronary distal pressure offset affects stenosis physiology appraisal. *Int. J. Cardiol.* **277**, 29–34, <https://doi.org/10.1016/j.ijcard.2018.08.051> (2019).
49. Menon, M., Jaffe, W., Watson, T. & Webster, M. Assessment of coronary fractional flow reserve using a monorail pressure catheter: the first-in-human ACCESS-NZ trial. *Eurointervention* **11**, 257–263, <https://doi.org/10.4244/Eijv11i3a51> (2015).
50. Cook, C. M. et al. Quantification of the effect of pressure wire drift on the diagnostic performance of fractional flow reserve, instantaneous wave-free ratio, and whole-cycle Pd/Pa. *Circ-Cardiovasc. Interv.* **9** (2016). <https://doi.org/10.1161/CIRCINTERVENTIONS.115.002988>